Supplemental Information for "Symmetry-reduced topological interface for unleashing a multidirectional spin-orbit torque"

Satoshi Sugimoto[1], Yasufumi Araki[2], Yukiko K. Takahashi[1], Jun'ichi Ieda[2], and Shinya Kasai[1*]

1. *Research Center for Magnetic and Spintronic Materials, National Institute for Materials Science, 1-2-1 Sengen, Tsukuba 305-0047, Japan*
2. *Advanced Science Research Center, Japan Atomic Energy Agency, Tokai, Ibaraki 319-1195, Japan*

(Dated: 06 February 2025)

[*]Corresponding author: KASAI.Shinya@nims.go.jp

Supplementary Note 1: Group-theory analysis of spin-orbit torque under wedging

Here we give a detailed theoretical discussion on the structure of spin-orbit torque (SOT) based on group theory. As we have taken in the main text, we take the Cartesian coordinate system (*X*, *Y*, *Z*) fixed to the crystal, with the *Z*-axis taken to the rotational symmetry axis (film normal). To understand the possible structure of the SOT, including the FL and DL components, we need to identify the form of spin polarization **S** that is carried by the spin current $\mathbf{J}_Z^{\mathrm{S}}$ flowing into the magnetic layer. [Note that the transformation properties of the spin current $\mathbf{J}_Z^{\mathrm{S}}$ and the spin polarization **S** under the symmetry operations in 2D space groups are identical, because of the broken mirror symmetry $(Z \rightarrow -Z)$ at the interface.] The possible structure of the induced **S** is given by constructing axial-vector components belonging to the irreducible representation of the space group in common with angular momentum, from the combinations of **E**, **m**, and any other inputs present in the system. In the following, we review the structure of SOTs permitted under the continuous group $\mathrm{C}_{\infty\mathrm{v}}$ and the threefold discrete group $\mathrm{C}_{3\mathrm{v}}$, as already known in previous literature. Then, we proceed to the SOTs newly emerging from the in-plane vector perturbation **F**, corresponding to the thickness gradient.

The continuous group $\mathrm{C}_{\infty\mathrm{v}}$ consists of two types of symmetry operations: (i) arbitrary rotation R_ϕ by angle ϕ around the *Z*-axis, and (ii) reflection σ_{v} by ∞-fold mirror planes sharing the *Z*-axis. Under these symmetry operations, the irreducible representations are also ∞-fold, as shown in the character table of Table SI. The 2D Dirac Hamiltonian,

$$H_{\infty\mathrm{v}}(\mathbf{k}) = v(k_X\sigma_Y - k_Y\sigma_X), \quad \text{(S1)}$$

is one of the typical forms belonging to $\mathrm{C}_{\infty\mathrm{v}}$, where $\sigma_{X,Y,Z}$ are the Pauli matrices for the electron spin degrees of freedom. This form describes the low-energy electrons on the surface of topological insulator at the lowest order in **k**, $O(k)$, which is subject to the isotropic energy-momentum dispersion and spin-momentum locking structure, as shown in Fig. 1a. The components of the vector **E** and the axial vector **m** transform by the symmetry operations as

$$R_\phi:\begin{pmatrix}E_X\\E_Y\\0\end{pmatrix}\rightarrow\begin{pmatrix}E_X\cos\phi - E_Y\sin\phi\\E_X\sin\phi + E_Y\cos\phi\\0\end{pmatrix},\qquad \begin{pmatrix}m_X\\m_Y\\m_Z\end{pmatrix}\rightarrow\begin{pmatrix}m_X\cos\phi - m_Y\sin\phi\\m_X\sin\phi + m_Y\cos\phi\\m_Z\end{pmatrix},$$

$$\sigma_{\mathrm{v}}:\begin{pmatrix}E_X\\E_Y\\0\end{pmatrix}\rightarrow\begin{pmatrix}E_X\\-E_Y\\0\end{pmatrix},\ \begin{pmatrix}m_X\\m_Y\\m_Z\end{pmatrix}\rightarrow\begin{pmatrix}-m_X\\m_Y\\-m_Z\end{pmatrix},\quad \text{(S2)}$$

where the mirror plane of σ_{v} is fixed to the *XZ*-plane. While (E_X, E_Y) and (m_X, m_Y) belong to the same two-dimensional irreducible representation E_1, their transformation properties under σ_v are different. To obtain an axial vector from the vector $\mathbf{E}$, we need to make a vector product, $\hat{\mathbf{Z}} \times \mathbf{E}$. In addition to this, by combining $\mathbf{E}$ and $\mathbf{m}$, we obtain $\mathbf{E}m_Z$ for the E_1 axial vector, corresponding to the *XY*-components of spin, and $\mathbf{E} \cdot \mathbf{m}$ for the A_2 axial vector, corresponding to the *Z*-component of spin. Therefore, the possible form of the spin polarization under $\mathrm{C}_{\infty\mathrm{v}}$ reads

$$\mathbf{S}_{\infty\mathrm{v}} = \chi_{\infty\mathrm{v}}^{(1)}\left(\hat{\mathbf{Z}} \times \mathbf{E}\right) + \chi_{\infty\mathrm{v}}^{(2)} m_Z \mathbf{E} + \chi_{\infty\mathrm{v}}^{(3)} (\mathbf{E} \cdot \mathbf{m})\hat{\mathbf{Z}}, \qquad \text{(S3)}$$

with arbitrary coefficients $\chi_{\infty\mathrm{v}}^{(1-3)}$. As far as the 2D interface with the isotropic Rashba SOC is concerned, the first term accounts for the FL-SOT from the Rashba-Edelstein effect. The second term accounts for the DL-SOT from the intrinsic effect, arising from the momentum-space Berry curvature. The third term is also classified as the DL-SOT, while the Rashba SOC does not yield this type of SOT, because the spin polarization of the Rashba SOC is limited in-plane. It is permitted under the hexagonally-warped SOC, and hence we denote the third term as $\mathbf{S}_{3\mathrm{v}}^{Z}$.

We next consider the discrete group $\mathrm{C}_{3\mathrm{v}}$, corresponding to the hexagonal crystalline interface such as $\mathrm{Bi_2Te_3}$ (001) employed in our experiment. This group contains the identity operation *E*, the threefold rotation R_3 around the *Z*-axis, and the reflection σ_v under the threefold mirror planes. The character table of $\mathrm{C}_{3\mathrm{v}}$ is shown in Table SII. As mentioned in the main text, we fix the coordinate system so that one of the mirror planes coincides with the *XZ*-plane; in hexagonal crystals, *X*, *Y*, and *Z* corresponds to $[\bar{1}10]$, $[110]$, and $[001]$ directions respectively. In particular, for the (001) surface of the topological insulator compound $\mathrm{Bi_2Te_3}$, its low-energy Hamiltonian is given as

$$H_{3\mathrm{v}}(\mathbf{k}) = H_{\infty\mathrm{v}}(\mathbf{k}) + \lambda\sigma_Z \operatorname{Re}(k_X + ik_Y)^3, \quad \text{(S4)}$$

where the second term reduces the symmetry from $\mathrm{C}_{\infty\mathrm{v}}$ to $\mathrm{C}_{3\mathrm{v}}$ and leads to the hexagonal warping of the spin-momentum locking structure, as shown in Fig. 1b. Under the rotational and mirror symmetry operations, the components of the vector ***E*** and the axial vector ***m*** transform as

$$R_\phi : \begin{pmatrix} E_X \\ E_Y \\ 0 \end{pmatrix} \to \begin{pmatrix} -\frac{1}{2}E_X - \frac{\sqrt{3}}{2}E_Y \\ \frac{\sqrt{3}}{2}E_X - \frac{1}{2}E_Y \\ 0 \end{pmatrix}, \quad \begin{pmatrix} m_X \\ m_Y \\ m_Z \end{pmatrix} \to \begin{pmatrix} -\frac{1}{2}m_X - \frac{\sqrt{3}}{2}m_Y \\ \frac{\sqrt{3}}{2}m_X - \frac{1}{2}m_Y \\ m_Z \end{pmatrix},$$

$$\sigma_\mathrm{v} : \begin{pmatrix} E_X \\ E_Y \\ 0 \end{pmatrix} \to \begin{pmatrix} E_X \\ -E_Y \\ 0 \end{pmatrix}, \quad \begin{pmatrix} m_X \\ m_Y \\ m_Z \end{pmatrix} \to \begin{pmatrix} -m_X \\ m_Y \\ -m_Z \end{pmatrix}. \quad \text{(S5)}$$

By constructing the axial-vector components belonging to the irreducible representations A_2 and E, we obtain the form of ***S*** permitted under $\mathrm{C}_{3\mathrm{v}}$,

$$\mathbf{S}_{3\mathrm{v}} = \chi_{3\mathrm{v}} \begin{pmatrix} E_X m_X - E_Y m_Y \\ -E_X m_Y - E_Y m_X \\ 0 \end{pmatrix}, \quad \text{(S6)}$$

in addition to the conventional forms $\mathbf{S}_{\infty\mathrm{v}}$. This form yields the "3m torque" and the "planar Hall torque" identified in previous literature, as discussed in the main text.

In addition to the C_{3v} structure, we take into account the effect of film wedging. While the wedging is even under time-reversal operation, it breaks the rotational symmetry (R_3) of C_{3v}. Moreover, it also breaks the mirror symmetry (σ_v), unless the slope of the wedged interface is set along the mirror plane. These characters of symmetry breaking are the same as the electric field **E**, belonging to the two-dimensional irreducible representation E. Therefore, here we symbolically denote the effect of wedging as an in-plane vector perturbation **F**, whose direction is defined parallel to the gradient of the interface. The simplest form for such a perturbation at the lowest order in **k** is uniquely determined as $(\mathbf{F} \cdot \mathbf{k})\sigma_Z$. With this perturbation term, the effective Hamiltonian for (001) interface of Bi_2Te_3 with the film wedging reads

$$\begin{aligned} H_1(\mathbf{k}) &= H_{3\mathrm{v}}(\mathbf{k}) + (\mathbf{F} \cdot \mathbf{k})\sigma_Z \\ &= k_X(v\sigma_Y + F_X\sigma_Z) + k_Y(-v\sigma_X + F_Y\sigma_Z) + \lambda\sigma_Z \operatorname{Re}(k_X + ik_Y)^3. \quad \text{(S7)} \end{aligned}$$

As can be seen in the second line, the perturbation **F** tilts the spin polarization to the out-of-plane direction even at $O(k)$, which strongly modulates the spin-momentum locking structure, as shown in Fig. 1c. Such a large effect on the spin-momentum locking structure owes to the linear Dirac dispersion of the topological surface state. From the in-plane components of **E** and **F**, we can construct the following 4 linearly independent combinations:

$$\begin{gathered} D_0 = E_X F_X + E_Y F_Y = \mathbf{E} \cdot \mathbf{F} \\ D_X = E_X F_X - E_Y F_Y \\ D_Y = -E_X F_Y - E_Y F_X \\ D_Z = E_X F_Y - E_Y F_X = (\mathbf{E} \times \mathbf{F})_Z. \quad \text{(S8)} \end{gathered}$$

Here, D_0 behaves as a scalar belonging to A_1, (D_X, D_Y) behaves as an in-plane polar vector belonging to E, and D_Z behaves as an out-of-plane axial vector belonging to A_2. By using these notations, the possible form of the axial vector components at the orders of perturbation expansion of $O(E, F)$ and $O(E, F, m)$ are listed in Table SII. Thus, the possible form of the spin polarization **S** in addition to $\mathbf{S}_{\infty\mathrm{v}}$ and $\mathbf{S}_{3\mathrm{v}}$ becomes,

$$\mathbf{S}_1 = \chi_{1\parallel} \begin{pmatrix} -D_Y \\ D_X \\ 0 \end{pmatrix} + \chi_{1\perp} \begin{pmatrix} 0 \\ 0 \\ D_Z \end{pmatrix} = \chi_{1\parallel} \begin{pmatrix} E_X F_Y + E_Y F_X \\ E_X F_X - E_Y F_Y \\ 0 \end{pmatrix} + \chi_{1\perp} \begin{pmatrix} 0 \\ 0 \\ E_X F_Y - E_Y F_X \end{pmatrix} \quad \text{(S9)}$$

at $O(E,F)$, which corresponds to Eq. (1) in the main text. Furthermore, at $O(E,F,m)$, the forms

$$\tilde{\mathbf{S}}_1 = \eta_{1\parallel}^{(1)} \begin{pmatrix} D_X m_X - D_Y m_Y \\ -D_X m_Y - D_Y m_X \\ 0 \end{pmatrix} + \eta_{1\parallel}^{(2)} \begin{pmatrix} D_0 m_X \\ D_0 m_Y \\ 0 \end{pmatrix} + \eta_{1\parallel}^{(3)} \begin{pmatrix} -D_Z m_Y \\ D_Z m_X \\ 0 \end{pmatrix} + \eta_{1\parallel}^{(4)} \begin{pmatrix} D_X m_Z \\ D_Y m_Z \\ 0 \end{pmatrix}$$

$$+\eta_{1\perp}^{(1)} \begin{pmatrix} 0 \\ 0 \\ D_X m_X + D_Y m_Y \end{pmatrix} + \eta_{1\perp}^{(2)} \begin{pmatrix} 0 \\ 0 \\ D_0 m_Z \end{pmatrix} \quad \text{(S10)}$$

are also permitted.

If **E** and **F** are applied to the *X* and *Y* directions, respectively, $\mathbf{S}_1$ and $\tilde{\mathbf{S}}_1$ read

$$\mathbf{S}_1 = E_X F_Y \begin{pmatrix} \chi_{1\parallel} \\ 0 \\ \chi_{1\perp} \end{pmatrix}, \ \tilde{\mathbf{S}}_1 = E_X F_Y \begin{pmatrix} \left[\eta_{1\parallel}^{(1)} - \eta_{1\parallel}^{(3)}\right] m_Y \\ \left[\eta_{1\parallel}^{(1)} + \eta_{1\parallel}^{(3)}\right] m_X + \eta_{1\parallel}^{(4)} m_Z \\ -\eta_{1\perp}^{(1)} m_Y \end{pmatrix}. \quad \text{(S11)}$$

These forms give both the FL-SOT $[\mathbf{S}_{\mathrm{FL}} \propto \hat{\mathbf{X}}]$ and the DL-SOT $[\mathbf{S}_{\mathrm{DL}} \propto \mathbf{m} \times \hat{\mathbf{X}}]$ corresponding to the spin polarization parallel to the applied electric field (**E** || *X*). These torque components are not captured in either $\mathbf{S}_{\infty\mathrm{v}}$ or $\mathbf{S}_{3\mathrm{v}}$.

Therefore, to obtain the unconventional SOT with spin polarization parallel to **E**, one needs to introduce the wedge (or any other spatial inhomogeneity) **F** to break both the rotational and mirror symmetries in C_{3v}.

irreps	Characters			Possible forms for **S**	
	E	R_ϕ	σ_v	$O(E)$	$O(E,m)$
A$_1$	1	1	1		
A$_2$	1	1	-1	-	$\mathbf{m}\cdot\mathbf{E}$
E$_1$	1	$2\cos\phi$	0	$\hat{\mathbf{Z}}\times\mathbf{E}$	$m_Z\mathbf{E}$
E$_2$	1	$2\cos 2\phi$	0		
⋮					

Table SI. Character table of the space group C$_{\infty\mathrm{v}}$. The two columns on the right list up the possible axial-vector combinations belonging to each irreducible representation (A$_2$: out-of-plane component, E$_1$: in-plane component).

irreps	Characters			Possible forms for **S**			
	E	R_3	σ_v	$O(E)$	$O(E,m)$	$O(E,F)$	$O(E,F,m)$
A$_1$	1	1	1				
A$_2$	1	1	-1	-	$\mathbf{m}\cdot\mathbf{E}$	D_Z	$D_X m_X + D_Y m_Y, D_0 m_Z$
E	1	-1	0	$\hat{\mathbf{Z}}\times\mathbf{E}$	$m_Z\mathbf{E}$, $\begin{pmatrix} E_X m_X - E_Y m_Y \\ -E_X m_Y - E_Y m_X \end{pmatrix}$	$\begin{pmatrix} -D_Y \\ D_X \end{pmatrix}$	$\begin{pmatrix} D_X m_X - D_Y m_Y \\ -D_X m_Y - D_Y m_X \end{pmatrix}, \begin{pmatrix} D_0 m_X \\ D_0 m_Y \end{pmatrix}, \begin{pmatrix} -D_Z m_Y \\ D_Z m_X \end{pmatrix}, \begin{pmatrix} D_X m_Z \\ D_Y m_Z \end{pmatrix}$

Table SII. Character table of the space group C$_{3\mathrm{v}}$. The four columns on the right list up the possible axial-vector combinations belonging to each irreducible representation (A$_2$: out-of-plane component, E : in-plane component). $D_{0,X,Y,Z}$ are the combinations of the components of **E** and **F** defined in Eq. (S8).

Supplementary Note 2: Field-direction dependence of the ST-FMR signals

In this section, we show the derivation of Eqs. (2) and (3), which are used to analyze the field-direction dependence of the measured ST-FMR signals in the main text. Here we set the coordinate system (*x,y,z*) to the laboratory frame, with the *x*-axis taken to the direction of current injection (**E**).

First, we consider the magnetization dynamics induced by the SOT at microwave frequency Ω, which is governed by the Landau-Lifshitz-Gilbert equation,

$$\dot{\mathbf{m}}(t) = -\gamma \mathbf{m} \times \mathbf{H}_{\mathrm{eff}} + \alpha \mathbf{m} \times \dot{\mathbf{m}} + \boldsymbol{\tau}_{\mathrm{SOT}}(\mathbf{m}) \cos \Omega t. \quad \text{(S12)}$$

Here, the effective magnetic field $\mathbf{H}_{\mathrm{eff}}$ comes from the external magnetic field, magnetic anisotropy, etc. We denote its magnitude and direction as $\mathbf{H}_{\mathrm{eff}} = H(\cos\theta, \sin\theta, 0)$. The second term on the right-hand side accounts for the Gilbert damping, with the damping parameter α. The third term characterizes the effect of SOT, where the factor $\cos\Omega t$ comes from the injected ac current. As for $\boldsymbol{\tau}_{\mathrm{SOT}}$, we here consider the FL and DL contributions from all three spin components $(\tau_{i,\mathrm{FL}}, \tau_{i,\mathrm{DL}})$ $(i = x, y, z)$, and also the “3m” and “planar Hall” torque contributions $(\tau_{3\mathrm{m}}, \tau_{\mathrm{PH}})$ permitted in C_{3v} point group, as discussed in the previous section. Thus, $\boldsymbol{\tau}_{\mathrm{SOT}}$ is decomposed as,

$$\boldsymbol{\tau}_{\mathrm{SOT}}(\mathbf{m}) = \sum_{i=x,y,z} \left[\tau_{i,\mathrm{FL}} \mathbf{m} \times \hat{\mathbf{i}} + \tau_{i,\mathrm{DL}} \mathbf{m} \times (\mathbf{m} \times \hat{\mathbf{i}})\right] + \tau_{3\mathrm{m}} \mathbf{m} \times \tilde{\mathbf{m}} + \tau_{\mathrm{PH}} \mathbf{m} \times (\mathbf{m} \times \tilde{\mathbf{m}}), \quad \text{(S13)}$$

with $\tilde{\mathbf{m}} = (m_x, -m_y, m_z) = -\sigma_{\mathrm{v}} \mathbf{m}$, where σ_{v} is the mirror reflection in C_{3v}.

To consider the resonance solution, we linearize the LLG equation. By extracting $\mathbf{u}(t) = \mathbf{m}(t) - \mathbf{m}_0$, with $\mathbf{m}_0$ the ground-state magnetization pointing to $\mathbf{H}_{\mathrm{eff}}$, the linearized LLG equation becomes,

$$\dot{\mathbf{u}} + \gamma \mathbf{u} \times \mathbf{H}_{\mathrm{eff}} - \alpha \mathbf{m}_0 \times \dot{\mathbf{u}} = \boldsymbol{\tau}_{\mathrm{SOT}}(\mathbf{m}_0) \cos\Omega t. \quad \text{(S14)}$$

By decomposing $\mathbf{u} = u_\theta \hat{\boldsymbol{\theta}} + u_z \hat{\mathbf{z}}$, with $\hat{\boldsymbol{\theta}} = (-\sin\theta, \cos\theta, 0)$, $\boldsymbol{\tau}_{\mathrm{SOT}}(\mathbf{m}_0)$ is decomposed as

$$\boldsymbol{\tau}_{\mathrm{SOT}}(\mathbf{m}_0) = \tau_{\mathrm{SOT}}^{\theta} \hat{\boldsymbol{\theta}} + \tau_{\mathrm{SOT}}^{z} \hat{\mathbf{z}} \quad \text{(S15)}$$

$$\tau_{\mathrm{SOT}}^{\theta} = \tau_{x,\mathrm{DL}} \sin\theta - \tau_{y,\mathrm{DL}} \cos\theta - \tau_{z,\mathrm{FL}} + \tau_{\mathrm{PH}} \sin 2(\theta + \delta)$$

$$\tau_{\mathrm{SOT}}^{z} = -\tau_{x,\mathrm{FL}} \sin\theta + \tau_{y,\mathrm{FL}} \cos\theta - \tau_{z,\mathrm{DL}} - \tau_{3\mathrm{m}} \sin 2(\theta + \delta),$$

where δ is the misalignment angle between the current injection direction (*x*-axis) and the mirror plane of the crystal (*X*-axis).

By using these forms, the LLG equation (S12) can be written in the matrix form,

$$\begin{pmatrix} \partial_t & \gamma H + \alpha \partial_t \\ -\gamma H - \alpha \partial_t & \partial_t \end{pmatrix} \begin{pmatrix} u_\theta(t) \\ u_z(t) \end{pmatrix} = \cos\Omega t \begin{pmatrix} \tau_{\mathrm{SOT}}^{\theta} \\ \tau_{\mathrm{SOT}}^{z} \end{pmatrix}. \quad \text{(S16)}$$

This equation can be solved algebraically, yielding the resonance solution

$$\begin{pmatrix} u_\theta(t) \\ u_z(t) \end{pmatrix} = \mathrm{Re}\,\frac{\mathrm{e}^{\mathrm{i}\Omega t}}{(\gamma H + \mathrm{i}\alpha\Omega)^2 - \Omega^2} \begin{pmatrix} \mathrm{i}\Omega & -\gamma H - \mathrm{i}\alpha\Omega \\ \gamma H + \mathrm{i}\alpha\Omega & \mathrm{i}\Omega \end{pmatrix} \begin{pmatrix} \tau^\theta_{\mathrm{SOT}} \\ \tau^z_{\mathrm{SOT}} \end{pmatrix}. \quad \text{(S17)}$$

By defining the resonance field strength $H_0 = \Omega/\gamma$ and the linewidth $\Delta = \alpha H_0$, we reach the relation

$$\frac{1}{(\gamma H + \mathrm{i}\alpha\Omega)^2 - \Omega^2} \begin{pmatrix} \mathrm{i}\Omega & -\gamma H - \mathrm{i}\alpha\Omega \\ \gamma H + \mathrm{i}\alpha\Omega & \mathrm{i}\Omega \end{pmatrix} = \frac{\gamma^{-1}}{(H + \mathrm{i}\Delta)^2 - H_0^2} \begin{pmatrix} \mathrm{i}H_0 & -H - \mathrm{i}\Delta \\ H + \mathrm{i}\Delta & \mathrm{i}H_0 \end{pmatrix}.$$

By assuming $|H - H_0|, \Delta \ll H_0$, this form can be further reduced as

$$\frac{1}{(H + \mathrm{i}\Delta)^2 - H_0^2} \begin{pmatrix} \mathrm{i}H_0 & -H - \mathrm{i}\Delta \\ H + \mathrm{i}\Delta & \mathrm{i}H_0 \end{pmatrix} \approx \frac{1}{2\Delta}\left[F_{\mathrm{Asym}}(H) - \mathrm{i}F_{\mathrm{Sym}}(H)\right] \begin{pmatrix} \mathrm{i} & -1 \\ 1 & \mathrm{i} \end{pmatrix},$$

with the Lorentzian and anti-Lorentzian factors

$$F_{\mathrm{Sym}}(H) = \frac{\Delta^2}{(H - H_0)^2 + \Delta^2}, \qquad F_{\mathrm{Asym}}(H) = \frac{\Delta(H - H_0)}{(H - H_0)^2 + \Delta^2}.$$

(S18)

Therefore, by applying the above relations to Eq. (S17), the resonance solution becomes

$$\begin{pmatrix} u_\theta(t) \\ u_z(t) \end{pmatrix} = \frac{1}{2\gamma\Delta} \mathrm{Re}\, \mathrm{e}^{\mathrm{i}\Omega t}\left[F_{\mathrm{Asym}}(H) - \mathrm{i}F_{\mathrm{Sym}}(H)\right] \begin{pmatrix} \mathrm{i} & -1 \\ 1 & \mathrm{i} \end{pmatrix} \begin{pmatrix} \tau^\theta_{\mathrm{SOT}} \\ \tau^z_{\mathrm{SOT}} \end{pmatrix}$$

$$= \frac{1}{2\gamma\Delta} \begin{pmatrix} -F_{\mathrm{Asym}}(H)\sin\Omega t + F_{\mathrm{Sym}}(H)\cos\Omega t & -F_{\mathrm{Asym}}(H)\cos\Omega t - F_{\mathrm{Sym}}(H)\sin\Omega t \\ F_{\mathrm{Asym}}(H)\cos\Omega t + F_{\mathrm{Sym}}(H)\sin\Omega t & -F_{\mathrm{Asym}}(H)\sin\Omega t + F_{\mathrm{Sym}}(H)\cos\Omega t \end{pmatrix} \begin{pmatrix} \tau^\theta_{\mathrm{SOT}} \\ \tau^z_{\mathrm{SOT}} \end{pmatrix}.$$

(S19)

From the resonance solution obtained above, we now evaluate the voltage signal in the ST-FMR measurement. Assuming the anisotropic magnetoresistance $R_{xx}(\theta) = R_0 + R_{\mathrm{AMR}}\cos^2\theta$, the resistance under the FMR becomes time-dependent,

$$R_{xx}\big(\theta(t)\big) = R_0 + R_{\mathrm{AMR}}\cos^2[\theta + u_\theta(t)] \approx R_0 + R_{\mathrm{AMR}}\cos^2\theta + R_{\mathrm{AMR}}\sin 2\theta\ u_\theta(t).$$

Therefore, in the voltage signal in response to the ac current $I_0\cos\Omega t$,

$$V_x(t) = R_{xx}\big(\theta(t)\big) \times I_0\cos\Omega t,$$

the time-independent signal reads

$$V_{x,\mathrm{dc}} = \frac{R_{\mathrm{AMR}} I_0}{4\gamma\Delta}\sin 2\theta\left[F_{\mathrm{Sym}}(H)\tau^\theta_{\mathrm{SOT}} - F_{\mathrm{Asym}}(H)\tau^z_{\mathrm{SOT}}\right]. \quad \text{(S20)}$$

By substituting the forms of $\left(\tau^\theta_{\mathrm{SOT}}, \tau^z_{\mathrm{SOT}}\right)$ from Eq. (S15), the θ-dependences of the symmetric and antisymmetric parts of $V_{x,\mathrm{dc}}$ are given as

$$V_{\mathrm{Sym}} = \frac{R_{\mathrm{AMR}} I_0}{4\gamma\Delta}\sin 2\theta\left[\tau_{x,\mathrm{DL}}\sin\theta - \tau_{y,\mathrm{DL}}\cos\theta - \tau_{z,\mathrm{FL}} + \tau_{\mathrm{PH}}\sin 2(\theta + \delta)\right],$$

$$V_{\mathrm{Asym}} = \frac{R_{\mathrm{AMR}} I_0}{4\gamma\Delta}\sin 2\theta\left[-\tau_{x,\mathrm{FL}}\sin\theta + \tau_{y,\mathrm{FL}}\cos\theta - \tau_{z,\mathrm{DL}} - \tau_{3\mathrm{m}}\sin 2(\theta + \delta)\right].$$

(S21)

Supplementary Note 3: Microstructure analysis for Bi_2Te_3/CoFeB heterostructures

Crystal structures of sputtered Bi_2Te_3 thin film are comprehensively evaluated using x-ray diffraction profile (XRD, Fig. S1a), energy dispersive x-ray spectroscopy (EDS, Fig. S3), and nano-beam diffraction (NBD, Fig. S1b). The sharp characteristic peaks at the XRD profile in Fig. S1a indicate the robust c-axis orientations of $R\bar{3}m$ Bi_2Te_3 films. The cross-sectional TEM image in Fig. 2c convinces the clear rhombohedral structure with atomic-scale precision, which is also supported by the NBD pattern in Fig. S1b. In-plane crystal orientation can be understood from such NBD pattern, and the major configuration is identified as $Bi_2Te_3(11\bar{2}0)[0001] \parallel Al_2O_3(11\bar{2}0)[0001]$.

Besides, the epitaxial but island growth process of sputtering leads to minor misaligned grains as summarized in Fig. S2. Among four different NBD patterns obtained at various positions, only point 4 shows the spacing twice larger than those in the other three patterns. Such a variation in the diffraction periodicity is identified as 90° rotations of in-planes crystal orientation, labeled as

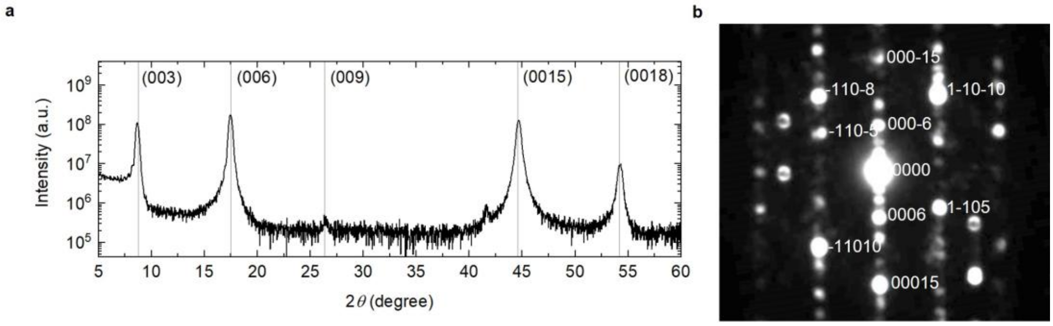

Fig. S1. Microstructure analysis of Bi_2Te_3 thin film. **a**, out-of-plane XRD profile. **b**, NBD pattern from Al_2O_3 [110] direction.

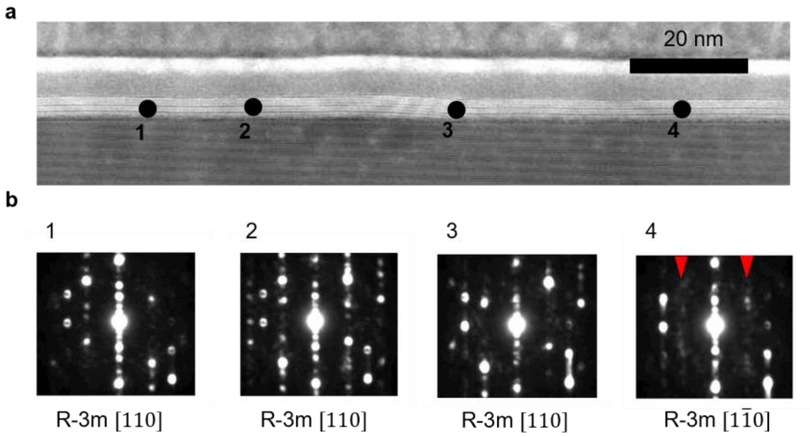

Fig. S2. NBD patterns from Al_2O_3[110] direction at different sample positions. **a**, cross-sectional TEM with four detection points. **b**, NBD patterns obtained at each detection point. Whereas the positions 1-3 indicate the alignment of the Bi_2Te_3-[110] direction along the Al_2O_3-[110] direction, only the position 4 loses intermediate streak lines (red triangles), indicating the in-plane crystal orientation of Bi_2Te_3 rotated to the [$1\bar{1}0$] direction along the Al_2O_3-[110].

$Bi_2Te_3(1\bar{1}00)[0001] \parallel Al_2O_3(11\bar{2}0)[0001]$. We investigated more than ten NBDs at different Bi_2Te_3 regions, and such in-plane rotated grains dominate around 20% of the major sample. Due to the coexistence of such rotated grains, it is difficult to distinguish the mirror axis [$\bar{1}10$] and the low-symmetry axis [110] of the Bi_2Te_3(001) plane in our experimental configurations. Such in-plane crystalline imperfection may make it difficult to distinguish the current injection directions between the mirror axis and the low-symmetry axis in the SOT measurement, which was successful in *the other low-symmetry materials,* WTe_2[1], $NbSe_2$[2] etc. Nevertheless, the above measurements imply that certain part of the current flows along the mirror axis [$\bar{1}10$] of Bi_2Te_3, which is the condition for realizing the trivial C_1 structure at the interface by the film wedging, as proposed in our symmetry reduction protocol.

Finally, the cross-sectional microstructure analyses of the whole Bi_2Te_3/CoFeB heterostructure are presented in Fig. S3. Layered Bi and Te atoms are clearly captured for both TEM and EDS images in Fig. S3a. More importantly, the cross-sectional EDS profile in Fig. S3b convinces an atomically steep interface between rhombohedral Bi_2Te_3 and amorphous CoFeB heterostructures. From these observations, we can conclude that our symmetry discussions based on the $R\bar{3}m$ structure of Bi_2Te_3 are quite reasonable in our sample using the sputtering fabrication approaches.

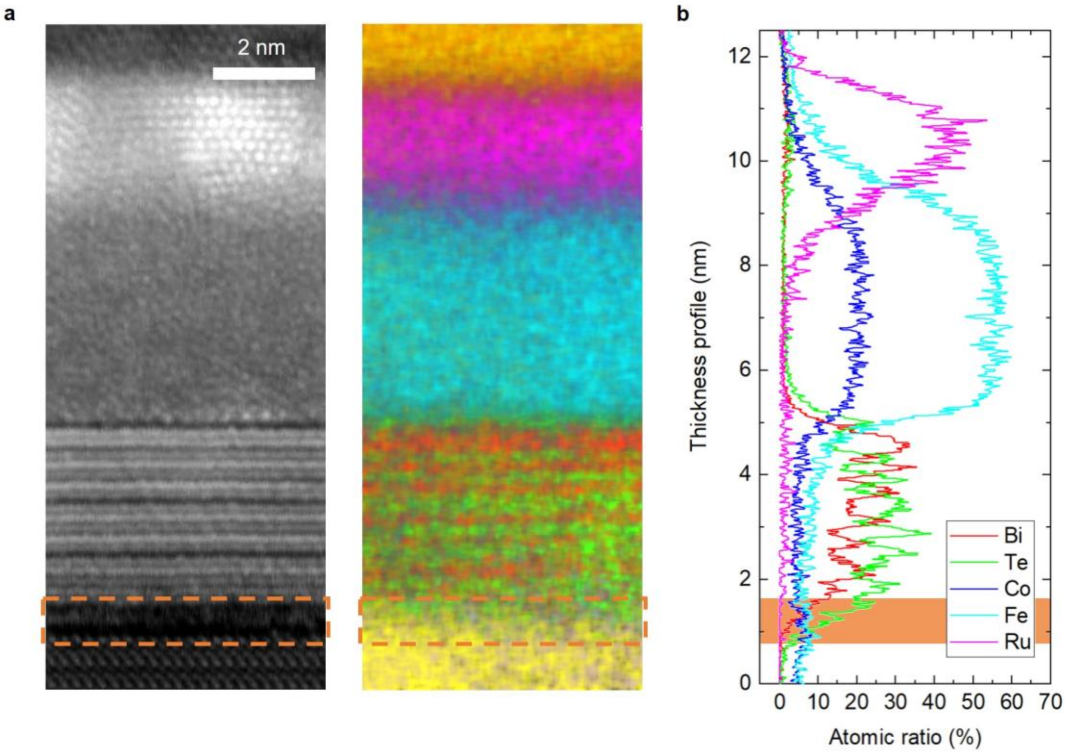

Fig. S3. **a**, Cross-sectional TEM (left) and EDS (right) images for Bi_2Te_3/CoFeB heterostructures. **b**, EDS profile of the constituent elements along thickness direction. The scale of the vertical axis is taken identical to the panel a. The orange dashed region in a and highlighted area in b exhibit an amorphous-like interface layer as reported by Tarakina et al. in Ref. 3.

Although high-quality epitaxial film growths are feasibly observed in our Bi_2Te_3/CoFeB heterostructures, we need to note that there still exist fundamental difficulties to obtain "perfect" C_{3V} structures for actual thin-film fabrications. We observe an amorphous-like interface layer as shown in enclosed and highlighted regions in Fig. S3a and b. Such monolayer-scale poor crystal quality interface layer suggests that many nucleation points are present at the very first stage of growth, and inevitable different stacking structures form finite twin boundaries in a Bi_2Te_3 epitaxial film[3]. Formations of twin boundaries prevent complete C_{3V} structures in microscale thin-film devices, which possibly cause huge variations in the conversion efficiencies in previous Bi-based chalcogenides reports (jumped from $\xi_{y,\mathrm{DL}} \sim o(1)$[4] to $o(100)$[5] for same $(Bi,Se)_2Te_3$).

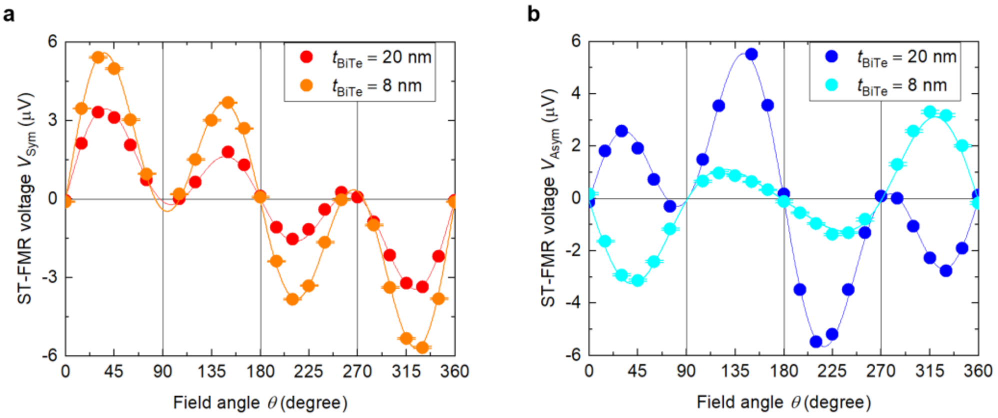

Fig. S4. Angular dependences of **a**. symmetric $\left(V_{\mathrm{Sym}}\right)$ and **b**, antisymmetric $\left(V_{\mathrm{Asym}}\right)$ components of ST-FMR signals observed in two different Bi_2Te_3 thicknesses; 20 nm thickness (red and blue symbols) and 8 nm thickness (orange and cyan symbols), respectively. The fitting curves are calculated based on Eqs. (2) and (3).

The effects of crystalline imperfection at thin film samples are implied also from our observation of the SOT efficiencies in the uniform-thickness Bi_2Te_3/CoFeB heterostructures. Figure S4 presents the SOT profiles in two different uniform Bi_2Te_3 film thicknesses (8 nm and 20 nm). By extracting the SOT components for each sample by the fitting to Eqs. (2) and (3), we find that the thick sample (20 nm) shows much weaker out-of-plane SOTs as $\left(\xi_{z,\mathrm{DL}}, \xi_{z,\mathrm{FL}}\right) = (-0.02 \pm 0.01, 0.00 \pm 0.00)$, with negligible parallel spin polarization $\left(\xi_{x,\mathrm{DL}}, \xi_{x,\mathrm{FL}}\right)$. On the other hand, the thin sample (8 nm) exhibit a clear deviation from the trivial SOT profiles, with the finite out-of-plane SOTs as $\left(\xi_{z,\mathrm{DL}}, \xi_{z,\mathrm{FL}}\right) = (-0.10 \pm 0.02, 0.06 \pm 0.01)$. The order of crystallinity in Bi-based chalcogenides is supposed to be sensitive to the total film thickness, where the thicker films tend to include more twinning and/or misalignment between neighboring hexagonal layers and/or grains. We expect that the thinner 8 nm sample is relatively free from such crystal imperfections, and capable of accessing the bulk C_{3V} properties compared to the 20 nm sample.

The imperfect C_{3V} structure should be caused also by a miscut of commercial sapphire substrates with tolerance of 0.1 degree. To relativize the effects of such imperfect crystalline alignment, we cut several pieces of 10 x 10 mm^2 substrate from the single 2-inch sapphire wafer, then fabricated uniform and wedge-shaped Bi_2Te_3/CoFeB heterostructures on the identical wafer condition.

We lastly note that observation of the finite anisotropic SOTs has not been a common insight for Bi_2Te_3 thin films so far. Although its C_{3V} structure enables the additional out-of-plane SOTs as deduced in Supplementary Note 1, none of the many previous works based on ST-FMR[6,7,8,9,10] mentioned their presence. The out-of-plane SOT measured in our sputtered thin films appears to be inconsistent with the previous reports, and hence we cannot immediately infer what is essential for these additional out-of-plane components. Nevertheless, our distinctive observations of strong in-plane and out-of-plane spin polarizations were reproduced by various experimental procedures; magnetization switching demonstrations (Supplementary Notes 7 and 8) and the 2nd harmonic measurement (Supplementary Notes 9), with convincing anisotropic behaviors in charge-to-spin conversion intrinsic to our platform. Furthermore, systematic observations with varying wedge thickness gradient and total film thickness were also successfully implemented (Supplementary Notes 10). For these reasons, even though our thin film Bi_2Te_3 samples are difficult to be identified as the perfect C_{3V} structure with atomic scale precision, we conclude that our symmetry reduction protocol by the thickness gradient has been reliably confirmed throughout comparisons among our three representative samples.

Supplementary Note 4: Contributions of spin pumping and the inverse Edelstein effect

Within a detection of ST-FMR as a charge-to-spin conversion process, its inversion process, i.e. spin-to-charge conversions, would also contribute the ST-FMR measurement. Contribution of spin pumping and the inverse Edelstein effect is developed by Mellnik et al.[11] as,

$$V_{\mathrm{SP}} = \xi_{y,\mathrm{DL}} \frac{ew\lambda_{\mathrm{TI}}R_{xx}}{2\pi} \tanh\left(\frac{t_{\mathrm{TI}}}{2\lambda_{\mathrm{TI}}}\right) \mathrm{Re}\left(g_{\uparrow\downarrow}^{\mathrm{eff}}\right) \langle (\mathbf{m} \times \dot{\mathbf{m}})_x \rangle, \qquad \text{(S22)}$$

where w presents the sample width, λ_{TI} does the spin conversion constant of Bi_2Te_3 layer, R_{xx} does the sample resistance, and $\mathrm{Re}\left(g_{\uparrow\downarrow}^{\mathrm{eff}}\right)$ does the real part of the effective spin mixing conductance. This contribution is superimposed only onto V_{Sym} as opposite to the original ST-FMR signal, and its in-plane profile is governed by the magnetization direction. This means in-plane angle dependence of V_{SP} is expected to be the same as conventional SOT contribution, following a rule of $\sin 2\theta \cos\theta$. Therefore, contribution of both spin pumping and the inverse Edelstein effect can be distinctive from quantitative estimations of $\xi_{x,\mathrm{DL(FL)}}$ and $\xi_{x,\mathrm{DL(FL)}}$, which draws completely different in their in-plane profiles as deduced in Eqs. (2) and (3).

A rough upper bound on $|V_{\mathrm{SP}}|$ can be estimated under feasible approximations as done in Ref. 4, with $\lambda_{\mathrm{TI}} \ll t_{\mathrm{TI}}/2$, $\mathrm{Re}\left(g_{\uparrow\downarrow}^{\mathrm{eff}}\right) \sim 10^{19}\mathrm{m}^{-2}$, and $\langle (\mathbf{m} \times \dot{\mathbf{m}})_x \rangle = \omega\phi_{\mathrm{p}}^2 \sin\theta \sqrt{\frac{\mu_0 H_0}{\mu_0 H_0 + M_{\mathrm{eff}}}}$ with the maximum precession angle ϕ_{p}. With the assumptions of $\phi_{\mathrm{p}} = \frac{1}{\mathrm{d}R/\mathrm{d}\theta}\frac{2}{I}\sqrt{V_{\mathrm{Sym}}^2 + V_{\mathrm{Asym}}^2} \ll 0.01$ and $\xi_{y,\mathrm{DL}} \ll 1$, we find an upper bound as $V_{\mathrm{SP}} \sim 2 - 4\mu\mathrm{V}$, which is almost half the order of V_{Sym} observed in Fig. 4c-f. We hence need to be careful of the conventional conversion efficiency $\xi_{y,\mathrm{DL}}$ for our Bi_2Te_3/FM heterostructure. Nevertheless, it does not affect our major conclusions of emergences of anisotropic SOT in this work.

Alternatively, Yang et al. have discussed enhanced contribution of spin pumping as proportional to a sinuous to the current projection, as $V_{\mathrm{SP}} \propto \sin\theta$ [12]. We quantified such sinuous phenomena as an additional term to Eq. (2). The estimated coefficient was smaller than $|\tau_{y,\mathrm{DL}}|$ by two orders, evaluated as a negligible contribution to both the conventional and anisotropic SOT.

Supplementary Note 5: Coefficients for the anisotropic SOT components

In Table SIII, we show the coefficients for the anisotropic SOT components, $(\tau_{x,\mathrm{DL}}, \tau_{y,\mathrm{DL}}, \tau_{z,\mathrm{DL}})$, $(\tau_{x,\mathrm{FL}}, \tau_{y,\mathrm{FL}}, \tau_{z,\mathrm{FL}})$, and $(\tau_{3\mathrm{m}}, \tau_{\mathrm{PH}})$, obtained from the fitting of the angular profiles of the ST-FMR spectra with the relations in Eqs. (2) and (3). It should be noted that their values are scaled by an overall factor for each heterostructure, and hence the magnitudes of the values cannot be compared between different heterostructures. This is because the overall factor depends on the details of the system such as the AMR ratio, the current density distribution, etc., which cannot be exactly determined.

	W/CoFeB	Uniform Bi_2Te_3/CoFeB	Wedged Bi_2Te_3/CoFeB
$\tau_{x,\mathrm{DL}}$	0	0.00 ± 0.00	1.50 ± 0.11
$\tau_{y,\mathrm{DL}}$	4.83 ± 0.24	-5.43 ± 0.16	-4.88 ± 0.15
$\tau_{z,\mathrm{DL}}$	0	2.05 ± 0.05	2.05 ± 0.07
$\tau_{x,\mathrm{FL}}$	0	0.00 ± 0.00	0.40 ± 0.08
$\tau_{y,\mathrm{FL}}$	2.57 ± 0.24	-0.61 ± 0.06	-3.07 ± 0.10
$\tau_{z,\mathrm{FL}}$	0	-1.42 ± 0.08	-1.67 ± 0.08
$\tau_{3\mathrm{m}}$	0	0.04 ± 0.08	-0.09 ± 0.10
τ_{PH}	0	0.08 ± 0.14	0.07 ± 0.14

Table SIII. Coefficients for the SOT components obtained from the fitting to Eqs. (2) and (3), for each heterostructure.

Supplementary Note 6: Effects of thermal components

Since sputtered Bi_2Te_3 is reported to work as a good thermoelectric (TE) material[13], series of current-induced heating effects need to be carefully discussed. Typical Joule heating effects on ST-FMR measurements have been investigated for conventional Pt[14] and its Cu binary alloys[15] so far. Inevitable temperature elevation is commonly explained by analogies with external stimulus for investigating the thermal dependence of spin conductance measurements, decrement in saturation magnetization of FM layer, small increase in the charge-to-spin conversion attributed to enhanced skew scattering effect, and increasement in energy loss exhibited in enhanced damping constant.

From the qualitative aspect, the thermal effect from the Joule heating does not affect the emergence of the unconventional SOT components discussed in the main text. This is because the out-of-plane temperature gradient from the Joule heating, which serves as the out-of-plane vector perturbation, does not alter the 2D point group structure at the interface. The symmetry arguments in Supplementary Note 1 apply even in the presence of the out-of-plane temperature gradient.

To quantify the temperature elevation by Joule heating, a low-power excitation of the ST-FMR at 5 dBm for wedge-shaped Bi_2Te_3/CoFeB heterostructures was tested as shown in Fig. S5a. The ST-FMR spectra is almost consistent with results with the general excitation conditions at 15 dBm in Fig. S5b except for the signal amplitude and noise level. This indicates that the dominant parameters related to the conversion process, including SOC amplitude and FM properties, were almost independent of the input power. The conversion efficiencies ξ_i $(i = x, y, z)$ in the low-power excitation are

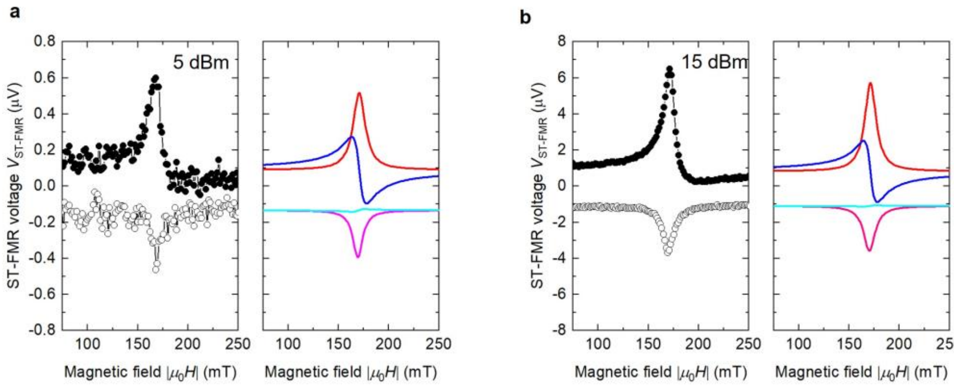

Fig. S5. ST-FMR voltage spectra with **a**, low-power excitation and **b**, reference spectra with general experimental conditions for wedge-shaped Bi_2Te_3 (8 nm + Δt)/CoFeB (5 nm) heterostructures.

estimated to be almost consistent with those from the conventional excitation within the difference around 5 %.

For these reasons, effects of thermal components of our works are estimated small enough to affect the major conclusions.

Supplementary Note 7: In-plane magnetization switching process by nonreciprocal SOT in Bi_2Te_3/CoFeB heterostructure

Due to the multidirectional SOT confirmed in the ST-FMR measurements in the main text, the magnetization switching process also becomes anisotropic. To demonstrate this, we have observed the switching of in-plane magnetization in the wedge-shaped heterostructure of Bi_2Te_3/CoFeB, which is visualized by the longitudinal magneto-optical Kerr effect (L-MOKE) microscopy images. The magnetization is initialized by the strong in-plane magnetic field $\mu_0 H = 100$ mT parallel to the current injection direction (Fig. S6a). After this initialization, the current pulse of 300 msec is injected, with its magnitude varied, and the magnetization profile is observed again. In comparison with the perfectly switched state (Fig. S6b), we find that the switched domain nucleation starts at current densities above $+6.3 \times 10^{10}\ \mathrm{A/m^2}$ without an external out-of-plane field (Fig. S6c-h), (see also Supplementary Note 8). From the magnetization profiles observed here, the normalized switched area is derived as a function of the current density and direction, as plotted in Fig. S6i. It increases with the current density, which indicates the deterministic switching process triggered by the multidirectional SOT free from the invariant points. Moreover, apart from the monotonic increase, the switched area under the negative current $j < 0$ is smaller than that under the positive current $j > 0$ by nearly 20 %. Such a difference is also seen by comparing Fig. S6c with S6d, S6e with S6f, or S6g with S6h, respectively. Such a direction-dependent switching behavior is barely observed in the SOT switching experiments, and apparently reflects the distinctively anisotropic SOT profile unique to symmetry-reduced (C_1) systems as visualized in Fig. 5a-c. These results, therefore, follow our ST-FMR measurement results discussed in the main text quantitatively.

Such in-plane SOT switching configuration shows analogies with type-x configuration in its current and magnetization directions, known to show advantages to switching speed and energy efficiency due to the reduced precession process[16]. The conventional SOT requires additional out-of-plane field application for the deterministic operation without the additional parallel spin polarization. The clear deterministic switching of in-plane magnetization in Fig. S6 supports our discussions of the finite in-plane polarization unleashed by the symmetry reduction, while the difficulties in generating in-plane polarization has prevented any experimental demonstrations of field-free type-x SOT operations except for a very few engineering reports[17] so far. Our anisotropic domain nucleation switching results would not meet the full demand of present SOT switching devices by themselves, but underlying concept of symmetry reduction would be feasibly applicable throughout further device optimizations.

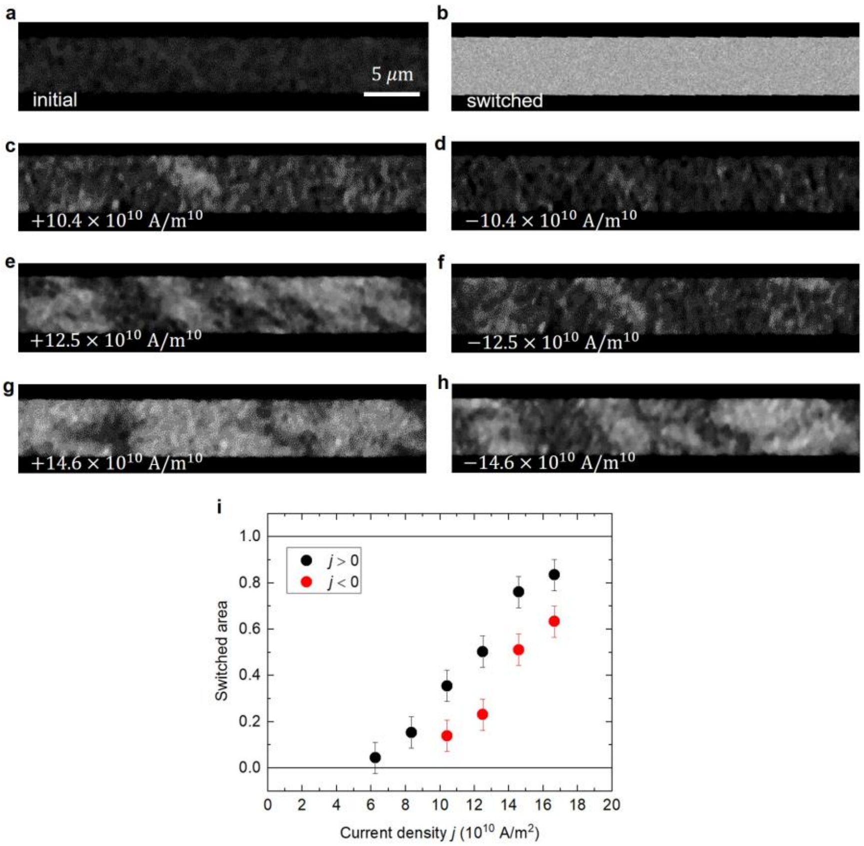

Fig. S6. Demonstrations of in-plane magnetization switching by anisotropic SOT. **a-h**, L-MOKE images of a wedge-shaped Bi_2Te_3 (8 nm + Δt)/CoFeB (5 nm) wire before and after 300 msec-dc pulse current injection. The current is injected orthogonally to the wedge direction, in the geometry same as that for the ST-FMR measurements in Fig. 3 and 4. Prior to the demonstrations, magnetization is initialized by a strong in-plane magnetic field $\mu_0 H = 100$ mT applied parallel to the current direction. The black region dominated in **a** indicates the magnetization along the positive field direction (initial state), and the light grey part dominated in **b** is for the magnetization along the negative field direction (switched state). **i**, Current density j-dependences of the switched area estimated from L-MOKE results. Black and red symbols indicate results for the positive $j > 0$ and the negative $j < 0$ current directions, respectively.

Supplementary Note 8: Domain nucleation process underlying in-plane magnetization switching in Bi_2Te_3/CoFeB heterostructure

Our measurements of the current-induced domain switching presented in Supplementary Note 7 are demonstrated in the domain nucleation regime. To distinguish the possible domain propagation processes during the domain switching, we have performed further experiments, with the continual current injections and/or modulations of pulse duration time.

A subtraction MOKE image under the sequential application of a negative current after a positive current ($+j \rightarrow -j$) is exhibited in Fig. S7a, and that of a positive current after a negative current ($-j \rightarrow +j$) is shown in Fig. S7b. The clear difference is observed only in the latter process ($-j \rightarrow +j$), which indicates that the secondary negative current in the former process does not induce domain propagation opposite to the positive current. These results clarify the anisotropy in spin polarization in the symmetry-reduced Bi_2Te_3/CoFeB heterostructure. Moreover, from these results, the domain nucleation processes are found to be dominant in the switching processes demonstrated in Supplementary Note 7, feasibly attributed to the strong pinning. The switched areas in the two processes ($+j \rightarrow -j$) and ($-j \rightarrow +j$) are presented in Fig. S7c, compared with $P_{+j} - P_{-j}$ from the single-pulse switched areas $P_{\pm j}$ measured in the main text. We find a good agreement between the switched area in the sequential process $-j \rightarrow +j$ and the popularity difference $P_{+j} - P_{-j}$ from the single-pulse processes. This agreement further supports the above discussions showing that the domain propagation is negligible.

The dominance of the domain nucleation process and strong pinning is also found from the measurements with subsequent pulse current injection, as shown in Fig. S7d-h. The partial domain switching is triggered only at the first pulse (see Fig. S7d), and the switched area stays almost unchanged up to the fifth pulse injection, as presented in Fig. S7i. These results indicate that the domain nucleation largely depends on the amplitude of the first current pulse, leaving the domain propagations by the subsequent pulses trivial.

The strong pinning of the domain walls is evidenced by the width broadening of the ST-FMR spectra in Fig. 3. Such a strong pinning probably owes to the grain misalignment and surface roughness in the Bi_2Te_3 film. Additional sample optimizations would be required to implement single-domain SOT switching.

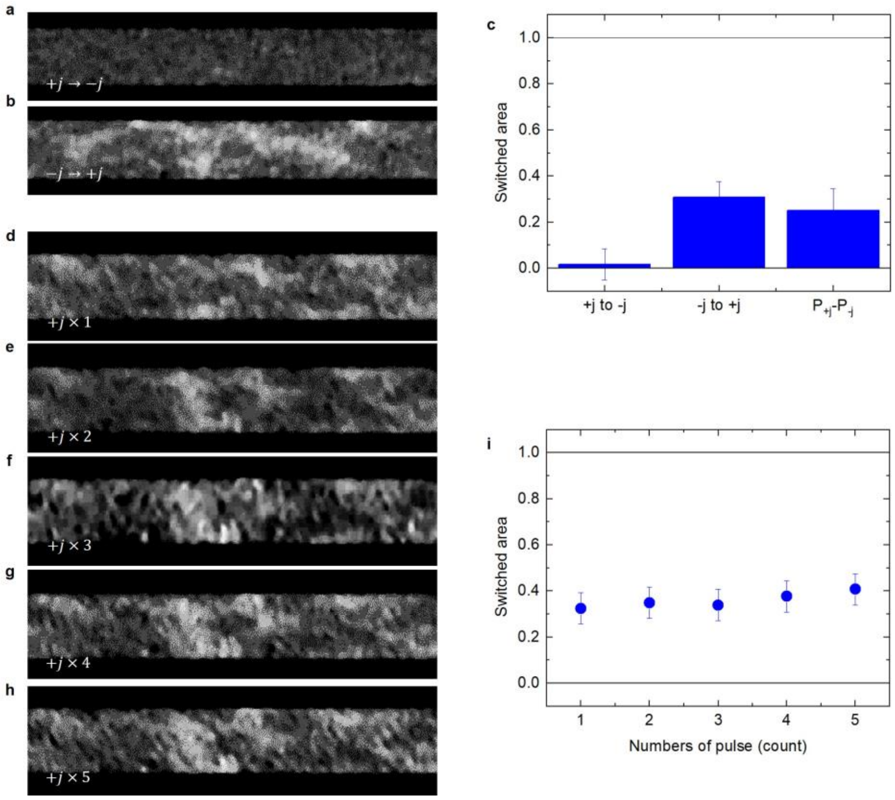

Fig. S7. Measurement results of the magnetization switching by sequential current pulse injections in the symmetry-reduced Bi_2Te_3/CoFeB heterostructures. **a-b**, Subtraction MOKE images with a negative current injection after a positive current $+j \rightarrow -j$ (**a**), and a positive current injection after a negative current $-j \rightarrow +j$ (**b**). **c**, Switched areas of subtraction processes $+j \rightarrow -j$, $-j \rightarrow +j$, and a difference of the single-pulse switched areas $P_{+j} - P_{-j}$. **d-h**, MOKE images with the subsequent current pulse injections up to five times. **i**, Switched areas with the subsequent current pulse injections. The current amplitude is set to $|j| = 10.4 \times 10^{10}\ \mathrm{A/m^2}$ with 300 msec in its duration time.

Supplementary Note 9: Second-harmonic Hall measurements for Bi$_2$Te$_3$/CoFeB heterostructures

Second-harmonic measurements of the Hall voltage[18,19,20,21] are also performed as the alternative approach to access the SOT in the symmetry-reduced Bi$_2$Te$_3$/CoFeB heterostructure, apart from the ST-FMR (main text) and the SOT-induced switching (Supplementary Note 7 and 8). Generalizing the argument in Refs. 22 and 23 by including the contributions of the in-plane and out-of-plane SOT components ($\tau_{\mathrm{SOT}}^{\theta}, \tau_{\mathrm{SOT}}^{z}$), the second-harmonic Hall resistivity is written as

$$R_{xy}^{2\omega} = \frac{R_{\mathrm{PHE}} \cos 2\theta\, \tau_{\mathrm{SOT}}^{z}}{\gamma \mu_0 H} + \frac{R_{\mathrm{AHE}} \cos\theta\, \tau_{\mathrm{SOT}}^{\theta}}{2\gamma(\mu_0 H + \mu_0 M_{\mathrm{eff}})} + \frac{V_{\mathrm{ANE}}}{I_0} \cos\theta, \qquad \text{(S23)}$$

where R_{PHE} and R_{AHE} are resistances of the planar Hall effect (PHE) and anomalous Hall effect (AHE), and V_{ANE} is the anomalous Nernst effect (ANE)-induced voltage arising from out-of-plane thermal gradient proportional to the Joule heating term $I^2 R$. θ is the angle of the in-plane magnetic field direction relative to the current flow.

Figure S8a shows the measurement results of the second harmonic Hall voltage in the Bi$_2$Te$_3$/CoFeB Hall bars as a function of the magnetic field $\mu_0 H$ angle θ against the current flow. The first two terms in Eq. (S22) are inversely proportional to the field strength, and hence the SOT-induced contributions are expected to decrease with increasing $\mu_0 H$. However, the measurement results for $50\ \mathrm{mT} \leq\ \mu_0 H \leq 5000\ \mathrm{mT}$ stays almost constant characteristics while showing sinusoidal manners against field rotation angle θ. These features indicate that the ANE contribution, the third term in Eq. (S22), is dominant in the second harmonic Hall voltage. This is because Bi$_2$Te$_3$ is known to show high thermoelectric efficiencies[24,25].

We now evaluate the SOT-induced contributions in the measured $R_{xy}^{2\omega}$. Under the condition $\mu_0 H \ll \mu_0 M_{\mathrm{eff}}$, the $\mu_0 H$-dependent part in $R_{xy}^{2\omega}$ becomes

$$\Delta R_{xy}^{2\omega} \approx \frac{\cos 2\theta}{\mu_0 H}(A_2 \sin\theta + A_1 \cos 2\theta + A_0), \qquad \text{(S24)}$$

with $A_0 = R_{\mathrm{PHE}} \tau_{z,\mathrm{DL}}/\gamma$, $A_1 = R_{\mathrm{PHE}} \tau_{y,\mathrm{FL}}/\gamma$, and $A_2 = R_{\mathrm{PHE}} \tau_{x,\mathrm{FL}}/\gamma$, where we have used the relation in Eq. (S15). The SOT efficiencies $\tau_{x,\mathrm{FL}}/\tau_{y,\mathrm{FL}}$ ($\tau_{z,\mathrm{DL}}/\tau_{y,\mathrm{FL}}$) can be determined independently from the fitting parameters as

$$\frac{A_2}{A_1} = \frac{\tau_{x,\mathrm{FL}}}{\tau_{y,\mathrm{FL}}} = \xi_{x,\mathrm{FL}}, \quad \frac{A_0}{A_1} = \frac{\tau_{z,\mathrm{DL}}}{\tau_{y,\mathrm{FL}}} = \xi_{z,\mathrm{DL}}. \text{(S24)}$$

The θ-dependent behavior of $\Delta R_{xy}^{2\omega}$ at $\mu_0 H = 50$ Oe, which is obtained by subtracting $R_{xy}^{2\omega}$ measured at the reference field of 5000 Oe, is plotted in Fig. S8b. This behavior agrees with Eq. (S23) by using the parameters obtained by the ST-FMR measurements, $\xi_{x,\mathrm{FL}} = -0.02$ and $\xi_{z,\mathrm{DL}} = -0.10$, as shown by the red line in Fig. S8b. Therefore, we can conclude that the second-harmonic Hall measurements presented here and the ST-FMR evaluations in the main text indicate the consistent structure of the unconventional SOT. Note that this harmonic measurement would not be appropriate for the precise evaluations of nontrivial torque components for general thermoelectric materials.

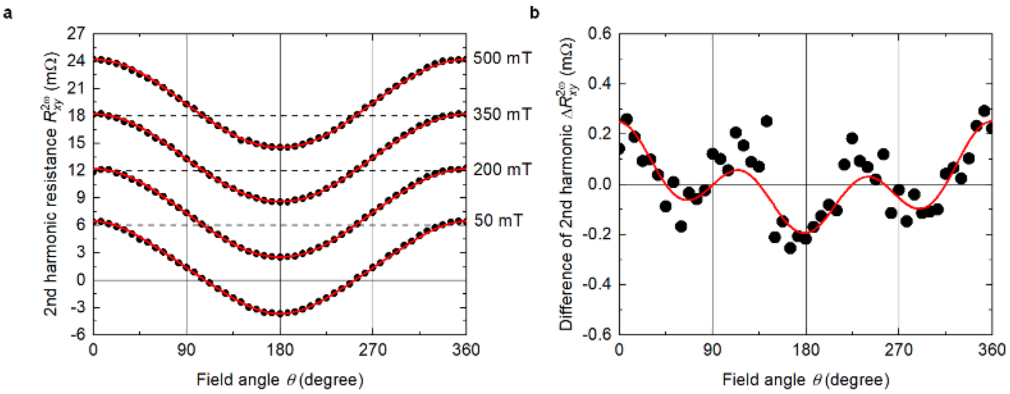

Fig. S8. Second-harmonic Hall measurement results in the symmetry-reduced Bi_2Te_3/CoFeB heterostructure. **a**, the in-plane field angle dependence of the second-harmonic Hall resistance. The fitting curves are calculated by Eq. (S22). **b**, the difference of second-harmonic voltage $\Delta R_{xy}^{2\omega}$, after removing the ANE contribution. The red solid line is the theoretically calculated behavior given by Eq. (S23), with the parameters given by the ST-FMR measurements in the main text.

Supplementary Note 10: Effects of wedge-gradient onto anisotropic SOTs

For our systematic understanding of the anisotropic SOTs, we conducted further investigations using various samples of Bi_2Te_3/CoFeB heterostructures with different (i) wedge structures and (ii) film thicknesses. The Bi_2Te_3/CoFeB heterostructures were uniformly patterned into bars with widths of 20 μm using photolithography techniques for three different wedge-gradients, $\Delta t = (5 \pm 1)$Å, labeled as [w5], (9 ± 2)Å as [w9] and (18 ± 3)Å as [w18]. The thickness t_{BiTe} at the center of Bi_2Te_3 were also varied from 6 nm to 20 nm. Except for systematic variation of Bi_2Te_3 wire design, experimental configurations are shared with those in Fig. 2d.

Figure S9 shows the parallel SOTs of wedged ([w5] ~ [w18]) and uniform thickness samples as functions of the center film thickness, in units of conversion efficiencies $\xi_{x,\mathrm{DL(FL)}}$. In consistent with the main results in Figs. 3 and 4, the finite parallel SOTs $\xi_{x,\mathrm{DL(FL)}}$ are obtained in wide thickness region for the wedge-fabricated samples. These anisotropic SOTs show a weak dependence on the thickness gradient, with the values of $|\xi_{x,\mathrm{DL(FL)}}|$ $(0.01 \ll |\xi_{x,\mathrm{DL(FL)}}| \leq 0.1)$ for [w18] in some samples larger than those for [w9]. Most importantly, such finite $|\xi_{x,\mathrm{DL(FL)}}| \neq 0$ turns to be negligible in the uniform thickness samples. By comparing these results with those from the uniform thickness samples, where $|\xi_{x,\mathrm{DL(FL)}}|$ is distinctively suppressed in both the 8 nm and 20 nm films, our measurements clearly indicate that the emergence of the

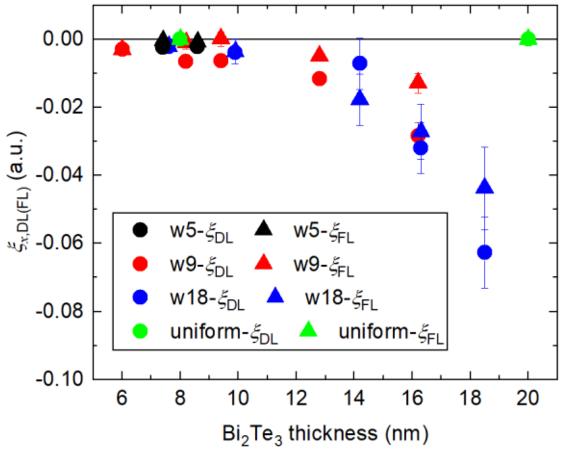

Fig. S9. Thickness dependence of parallel SOTs $\xi_{x,\mathrm{DL(FL)}}$ in units of conversion efficiencies. The different wedge-structure results as $\Delta t = (5 \pm 1)$Å (w5), (9 ± 2)Å (w9), and (18 ± 3)Å (w18) are indicated by black, red and blue circles or triangles, respectively. The uniform thickness results (uniform-$\xi_{\mathrm{DL(FL)}}$) are plotted by green circles or triangles as control experiments.

anisotropic parallel SOT components can be attributed to the implementation of thickness gradient in the Bi_2Te_3 thin films.

On the other hand, more quantitative understanding of the parallel SOTs remains yet to be established, concerning the data as far as we have. One concern is the weak dependence on the thickness gradient [w5] - [w18]. This indicates that the magnitude of the effective in-plane vector perturbation **F**, which linearly modulates $\left|\xi_{x,\mathrm{DL(FL)}}\right|$ as introduced in Eq. S11, is not necessarily proportional to the size of the thickness gradient. As another concern, we find the increase in the parallel SOTs with film thickness. To understand this behavior, we need to separate the effect of multi-grain formations in thicker Bi_2Te_3 samples, as discussed in Fig. S4 in Supplementary Note 3, which may cause non-vanishing anisotropic SOTs[26]. For the quantitative understandings on these concerns, further detailed studies of SOT experiments and microstructure analysis would be required, which are beyond the scope of this paper.

Supplementary References

---

[1] D. MacNeill, G. M. Stiehl, M. H. D. Guimaraes, R. A. Buhrman, J. Park, and D. C. Ralph, Nat. Phys. 13, 300–305 (2017).

[2] M. H. Guimarães, G. M. Stiehl, D. MacNeill, N. D. Reynolds, and D. C. Ralph, Nano Lett. 18, 1311–1316 (2018).

[3] N. V. Tarakina, S. Schreyeck, M. Luysberg, S. Grauer, C. Schumacher, G. Karczewski, Adv. Mater. Interfaces 1, 1400134 (2014).

K. Brunner, C. Gould , H. Buhmann , R. E. Dunin-Borkowski , and L. W. Molenkamp

[4] H. Wu, Y. Xu, P. Deng, Q. Pan, S. A. Razavi, K. Wong, L. Huang, B. Dai, Q. Shao, G. Yu, X. Han, J. C. Rojas-Sánchez, S. Mangin, and K. L. Wang, Adv. Mater. 31, 1901681 (2019).

[5] Y. Fan, P. Upadhyaya, X. Kou, M. Lang, S. Takei, Z. Wang, J. Tang, L. He, L.-T. Chang, M. Montazeri, G. Yu, W. Jiang, T. Nie, R. N. Schwartz, Y. Tserkovnyak, and K. L. Wang, Nat. Mater. 13, 699-704 (2014).

[6] Y. Wang, P. Deorani, K. Banerjee, N. Koirala, M. Brahlek, S. Oh, and H. Yang, Phys. Rev. Lett. 114, 257202 (2015).

[7] K. Kondou, R. Yoshimi, A. Tsukazaki, Y. Fukuma, J. Matsuno, K. S. Takahashi, M. Kawasaki, Y. Tokura, and Y. Otani, Nat. Phys. 12, 1027–1031 (2016).

[8] Y. Wang, D. Zhu, Y. Wu, Y. Yang, J. Yu, R. Ramaswamy, R. Mishra, S. Shi, M. Elyasi, K.-L. Teo, Y. Wu, and H. Yang, Nat. Commun. 8, 1364 (2017).

[9] F. Bonell, M. Goto, G. Sauthier, J. F. Sierra, A. I. Figueroa, M. V. Costache, S. Miwa, Y. Suzuki, and S. O. Valenzuela, Nano Lett. 20, 5893–5899 (2020).

[10] T. Manoj, Z. Wen, J. Uzuhashi, T. Ohkubo, H. Sukegawa, C. Murapaka, B. York, X. Liu, Q. Le, and S. Mitani, ACS Appl. Electron. Mater. 6, 4269–4276 (2024).

[11] A. R. Mellnik, J. S. Lee, A. Richardella, J. L. Grab, P. J. Mintun, M. H. Fischer, A. Vaezi, A. Manchon, E.-A. Kim, N. Samarth, and D. C. Ralph, Nature 511, 449–451 (2014).

[12] W. L. Yang, J.W. Wei, C. H. Wan, Y.W. Xing, Z. R. Yan, X. Wang, C. Fang, C. Y. Guo, G. Q. Yu, and X. F. Han, Phys. Rev. B 101, 064412 (2020).

[13] X. Han, Z. Zhang, Z. Liu, C. Xu, X. Lu, L. Sun, and P. Jiang, Appl. Nanosci. 10, 2375-2381 (2020).

[14] P. Phu, K. Yamanoi, K. Ohnishi, J. Hyodo, K. Rogdakis, Y. Yamazaki, T. Kimura, and

---

H. Kurebayashi, J. Magn. Magn. Mater. 485, 304-307 (2019).

[15] G. D. H. Wong, W. C. Law, F. N. Tan, W. L. Gan, C. C. I. Ang, Z. Xu, C. S. Seet, and W. S. Lew, Sci. Rep. 10, 9631 (2020).

[16] S. Fukami, T. Anekawa, C. Zhang, and H. Ohno, Nat. Nanotechnol. 11, 621–625 (2016).

[17] F. Xue, S.-J. Lin, M. Song, W. Hwang, C. Klewe, C.-M. Lee, E. Turgut, P. Shafer, A. Vailionis, Y.-L. Huang, W. Tsai, X. Bao, and S. X. Wang Nat. Commun. 14, 3932 (2023).

[18] K. Garello, I. M. Miron, C. O. Avci, F. Freimuth, Y. Mokrousov, S. Blügel, S. Auffret, O. Boulle, G. Gaudin, and & P. Gambardella, Nat. Nanotechnol. **8,** 587-593 (2013).

[19] M. Hayashi, J. Kim, M. Yamanouchi, and H. Ohno, Phys. Rev. B **89**, 144425 (2014).

[20] U. H. Pi, K. W. Kim, J. Y. Bae, S. C. Lee, Y. J. Cho, K. S. Kim, and S. Seo, Appl. Phys. Lett. **97**, 162507 (2010).

[21] J. Kim, J. Sinha, M. Hayashi, M. Yamanouchi, S. Fukami, T. Suzuki, S. Mitani, and H. Ohno, Nat. Mater. **12**, 240-245 (2013).

[22] C. O. Avci, K. Garello, M. Gabureac, A. Ghosh, A. Fuhrer, S. F. Alvarado, and P. Gambardella, Phys. Rev. B **90**, 224427 (2014).

[23] D. MacNeill, G. M. Stiehl, M. H. D. Guimaraes, R. A. Buhrman, J. Park, and D. C. Ralph, Nat. Phys. **13**, 300 (2017).

[24] M. Scheele, N. Oeschler, K. Meier, A. Kornowski, C. Klinke, and H. Weller, Adv. Funct. Mater. **19**, 3476 (2009).

[25] J. J. Shen, L. P. Hu, T. J. Zhu, and X. B. Zhao, Appl. Phys. Lett. **99**, 124102 (2011).

[26] M. DC, D.-F. Shao, V. D.-H. Hou, A. Vailionis, P. Quarterman, A. Habiboglu, M. B. Venuti, F. Xue, Y.-L. Huang, C.-M. Lee, M. Miura, B. Kirby, C. Bi, X. Li, Y. Deng, S.-J. Lin, W. Tsai, S. Eley, W.-G. Wang, J. A. Borchers, E. Y. Tsymbal, and S. X. Wang, Nat. Mater. 22, 591–598 (2023).